Check for updates

The role of the three body photodissociation channel of water in the evolution of dioxygen in astrophysical applications

Suming An,[a] Sukrit Ranjan, [ID] [bcde] Kaijun Yuan, [ID] [f] Xueming Yang [ID] *[fg] and
Rex T. Skodje [ID] *[a]

A recent experiment at the Dalian Coherent Light Source (DCLS) has provided measurements of the partial cross sections for the photodissociation of water vapor over an unprecedented range of wavelengths in the vacuum ultraviolet (VUV) region. It was found that the three body dissociation channel, H + H + O(^{3}P/^{1}D), becomes prominent at wavelengths shorter than the Lyman α-line at 121.6 nm. The present work explores the kinetic consequences of this discovery for several astrophysically motivated examples. The irradiation of a dilute low-temperature gas by unscreened solar radiation, similar to early stage photochemical processing in a comet coma, shows significant increase in the production of O_2-molecules at shorter times, <1 day, that might physically correspond to the photochemical reaction zone of the coma. Several examples of planetary atmospheres show increased O-atom production at high altitudes but relatively little modification of the equilibrium O_2 concentrations predicted by conventional models.

[a] *Department of Chemistry, University of Colorado, Boulder, CO 80309-215, USA.*
  E-mail: Rex.Skodje@colorado.edu
[b] *Department of Earth, Atmospheric & Planetary Sciences, Massachusetts Institute of*
  Technology, Cambridge, MA 02139, USA
[c] *Center for Interdisciplinary Exploration & Research in Astrophysics, Northwestern*
  University, Evanston, IL 60640, USA
[d] *Department of Physics & Astronomy, Northwestern University, Evanston, IL 60640,*
  USA
[e] *Blue Marble Space Institute of Science, Seattle, WA 98104, USA*
[f] *State Key Laboratory of Molecular Reaction Dynamics and Dalian Coherent Light*
  Source, Dalian Institute of Chemical Physics, Chinese Academy of Sciences,
  457 Zhongshan Road, Dalian, 116023, China
[g] *Department of Chemistry, College of Science, Southern University of Science and*
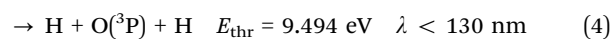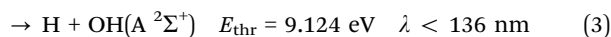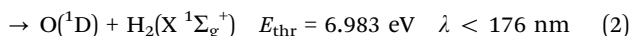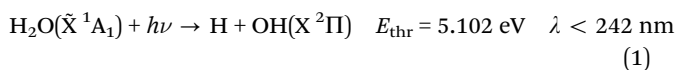 *Technology, Shenzhen 518055, China*

I. Introduction

The photodissociation of water has long been of interest to chemists as a prototype system for the photochemistry of triatomic molecules.[1–8] It also represents a fundamentally important process occurring in natural environments such as planetary atmospheres, dense interstellar molecular clouds, and comet comae.[9–11] Indeed, the empirical rates associated with this photochemistry are key parameters in many atmospheric and photochemical models.[12–14] Therefore, any significant improvements to the photodissociation cross sections may potentially lead to important practical changes in the predictions of those models. Here, we explore the implications of a recently investigated cross-section for the three body

dissociation process that occurs in the VUV region of the spectrum.[15]

There are several potential product channels available to the dissociating water molecule. The lowest energy triplet threshold occurs at 5.106 eV for the ground state product O(^{3}P) + H$_2$(X $^1\Sigma_g^+$), which, to be observed, requires a spin-forbidden transition from the initial singlet state of water, H$_2$O(X̃ ^{1}A$_1$). This channel is thus unimportant under most conditions. The lowest spin-allowed transitions of importance include the processes,

$$H_2O(\tilde{X}\,^1A_1) + h\nu \rightarrow H + OH(X\,^2\Pi) \quad E_{thr} = 5.102\ eV \quad \lambda < 242\ nm \tag{1}$$

$$\rightarrow O(^1D) + H_2(X\,^1\Sigma_g^+) \quad E_{thr} = 6.983\ eV \quad \lambda < 176\ nm \tag{2}$$

$$\rightarrow H + OH(A\,^2\Sigma^+) \quad E_{thr} = 9.124\ eV \quad \lambda < 136\ nm \tag{3}$$

$$\rightarrow H + O(^3P) + H \quad E_{thr} = 9.494\ eV \quad \lambda < 130\ nm \tag{4}$$

$$\rightarrow H + O(^1D) + H \quad E_{thr} = 11.46\ eV \quad \lambda < 108\ nm \tag{5}$$
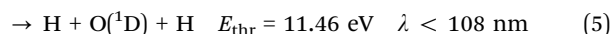
The relative contributions of these processes to the photochemistry are functions of wavelength and reflect the detailed nonadiabatic dynamics occurring on excited state surfaces. The absorption spectrum of ground state H$_2$O is shown in Fig. 1.[16–18] A schematic diagram of the electronic surfaces associated with some of these absorption features is presented in Fig. 2. The photodissociation from the low energy band centered in the range 140–190 nm corresponds to dynamics following the electronic transition Ã ^{1}B$_1$ ← X̃ ^{1}A$_1$. The dynamics induced by transitions in

This journal is © the Owner Societies 2021
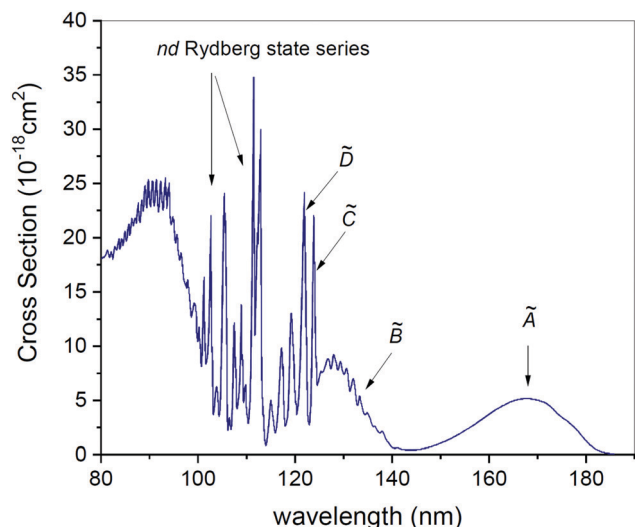
Phys. Chem. Chem. Phys., 2021, **23**, 9235–9248 | 9235

Fig. 1 The total absorption cross section for H$_2$O measured at T = 22 °C as adapted from ref. 16.

this spectral range have been extensively studied and are understood as simple direct dissociation on the Ã potential energy surface which dominantly yields the product channel H + OH(X$^2\Pi$) (*i.e.* process 1 above). The second continuum, peaked at ∼128 nm, has also been studied both theoretically and experimentally and all the allowed open product channels are accessed to some degree. For this B̃-state band, the photodissociation is mediated through the B̃ ^{1}A$_1$ ← X̃ ^{1}A$_1$ transition, followed by a variety of internal conversion processes that couple together the B̃, Ã, and X̃ states of water. The resulting spectrum is structured as are the chemical branching ratios. The largest product channel remains H(^{2}S) + OH(X$^2\Pi$), but the products H + OH(A $^2\Sigma^+$), O(^{1}D) + H$_2$(X $^1\Sigma_g^+$), and H + H + O(^{3}P) become significant. The Lyman-α line at λ = 121.6 nm has been most heavily studied where the experimental product branching is reported as to be 0.64, 0.11, 0.14, and 0.11 for processes 1, 2, 3, and 4 respectively.[3,19] Shorter wavelengths will involve higher Rydberg states with more complex nonadiabatic dynamics, C̃ ^{1}B$_1$ ← X̃ ^{1}A$_1$, D̃ ^{1}A$_1$ ← X̃ ^{1}A$_1$, *etc.*[20] Since these branching fractions are strong functions of the nonadiabatic coupling, and given the highly structured spectrum observed in Fig. 1, we should expect that the product distributions will likewise exhibit strong and structured wavelength dependence. The theoretical modeling on the lowest three surfaces certainly predicts such behavior.[4,5]

Recently, a new tool has been developed for the study of molecular photochemistry, the intense VUV free electron laser (FEL) at the Dalian Coherent Light Source (DCLS).[21–24] This device yields a tunable VUV source that permits the study of the photodissociation dynamics throughout the entire VUV region.

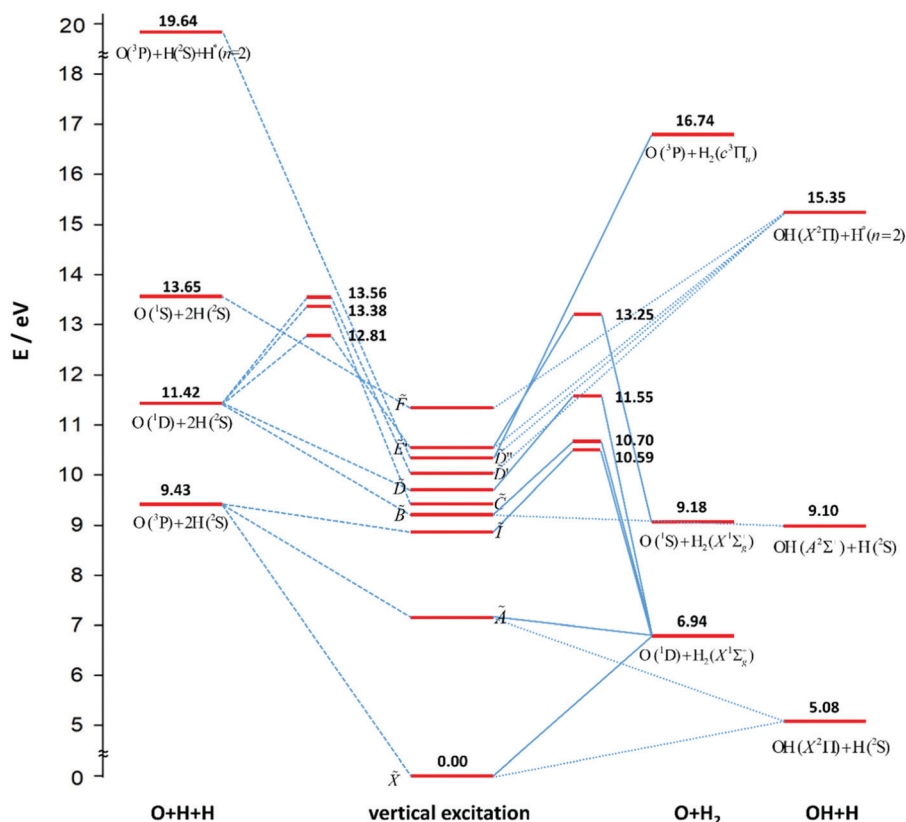Fig. 2 A schematic diagram showing the Rydberg progression of H$_2$O states and the available dissociation channels. Some of the zero-point corrected adiabatic barriers that correlate to the various excited states are shown. The results are calculated using a high level MRCI procedure described elsewhere.[40]

9236 | *Phys. Chem. Chem. Phys.*, 2021, **23**, 9235–9248

This journal is © the Owner Societies 2021

Combined with the H-atom Rydberg tagging time-of-flight (HRTOF) detection technique, the cross sections for major binary and three body dissociation channels can be measured directly. Interestingly, the three body dissociation channel (process 4) is found to be much larger than expected in the range 90–110 nm. While the total absorption cross section of H_2O is similar to that obtained previously, the branching ratios in the high energy regime are quite different than those at the Lyman-α line. In fact, the three body dissociation channel become dominant at these low wavelengths. At 107 nm the O + H + H channel (processes 4 and 5) constitute 67% of the products and by 92 nm they comprise 86% of all dissociation products. The precise dynamical mechanism underlying this result remains obscure at the moment due to the complexity of the nonadiabatic dynamics. However, a careful examination of the HRTOF data suggests that the production of O-atoms may occur by a sequential process, $H_2O + h\nu \rightarrow H + OH^\star \rightarrow H + H + O$ where $OH^\star$ is short lived intermediate. For our discussion, a knowledge of the dynamical mechanism is not required since we shall focus on the kinetics implied by the observed cross sections.

The growth of the three body channel at high energy suggests that the photochemical rate of oxygen atom production may be significantly enhanced in environments where VUV is relatively plentiful. This in turn could affect the production of important stable species such as O_2. The major thrust of the present work is to consider how the new cross section may affect the outcome of modeling in atmospheric and astrophysical applications. In particular, we investigated the chemical evolution of comet comae using a simple photochemical kinetics model and that of several planetary atmospheres using a more detailed representation of the full chemical and transport processes. We note that the outcome of such modeling efforts will be the net result of several competing factors. While the new cross sections predict a much larger production rate of atomic oxygen in the VUV region, there is relatively little such light in the solar spectrum. Furthermore, the increased production of hydrogen atoms will tend to balance the effect of oxygen through chemical equilibration processes in many practical environments.[11] We shall see some observable effects of the enhanced three body dissociation process for environments rich in VUV and H_2O vapor, such as comet comae, and substantially less effect for screened and highly equilibrated environments such as exist with most stable atmospheres.

The possible abiotic generation O_2 in planetary atmospheres has been a particularly active area of investigation.[25–27] The detection of significant O_2 concentrations in the spectral signatures from exoplanets is a possible signal of extraterrestrial life. However, the photochemical abiotic generation of O_2 yields a false positive to such a test. Therefore, it is of importance to determine under what circumstances molecular oxygen is created in detectable amounts through the irradiation of lifeless atmospheres. As a related issue, it is also of great interest to use modeling to theoretically predict whether O_2 may have been present in the early Earth atmosphere before life evolved. The primary photochemical instigator of O_2 creation in many abiotic planetary atmospheres is

presumed to be the photolysis of either H_2O or CO_2 gases. For the CO_2 precursor, the O_2 is formed from O-atom recombination with the assistance of a third body, $i.e.$, $O + O + M \rightarrow O_2 + M$. The H_2O photolysis to OH + H leads to O_2 through various catalytic cycles but appears to be ultimately rate limited by the elimination of hydrogen from the environment by, $e.g.$ escape into outer space. The potential of significant three body dissociation of water is intriguing since then the O-atoms are directly generated and can recombine. Of course the question of hydrogen balance is still important and modeling is required in a way that preserves redox balance.

In Section II, the modeling procedure employed here is described. The irradiation of the comet coma is described by a simple plug flow reactor with a comprehensive list of photochemical and secondary reactions along with grain chemistry. The chemistry is described as a function of time, which then is related to distance from the nucleus. The planetary atmospheres are described using a comprehensive photochemical-transport model described by Hu $et\ al.$[28] In Section III the results are presented. The plug flow kinetics is analyzed using sensitivity analysis and the origin of the O_2 species is described mechanistically. The results of the planetary simulation of modern Earth, modern Mars, and early Earth is presented. Only very small changes in the atmospheric chemical compositions are observed. Section IV concludes and summarizes the results.

II. Modeling

The chemical production rate into a given photodissociation channel is governed by the familiar expression for the J-value, here indexed by i,

$$J_i^{H_2O} = \int \sigma_i^{H_2O}(\lambda, T) \cdot I(\lambda) d(\lambda)$$

where $\sigma_i(\lambda,T)$ is the appropriate partial cross section for an equilibrium distribution of water molecules at temperature T, which is related to the total absorption cross section by the quantum yield $\sigma_i(\lambda,T) = \Phi_i(\lambda,T)\sigma_{tot}(\lambda,T)$. We assume for this discussion that the water molecule lies in the ground state so the temperature dependence can be dropped. The quantity $I(\lambda)$ is the available light intensity per unit wavelength. The $J_i^{H_2O}$ values for production in the channels $OH(X^2\Pi) + H$ and $OH(A^2\Sigma) + H$ are combined to a single rate for ground state product, $OH(X^2\Pi) + H$. This assumes that the excited state lifetime due to fluorescence and collisional quenching is short on the timescale of chemical modeling. We likewise assume the three body channel is dominated by the product $H + H + O(^3P)$. Since the detailed branching into processes 4 and 5 have not been clearly established by experiment, this seems a reasonable choice, even though $O(^1D)$ more reactive than $O(^3P)$. In Fig. 3 we show the low temperature limit of the total absorption cross section $\sigma_{tot}(\lambda)$ and the three body partial cross section $\sigma_4(\lambda)$ over a broad range of wavelengths. The difference between these two curves is identified with the products H + OH, $i.e.$, $\sigma_1(\lambda) + \sigma_3(\lambda)$.

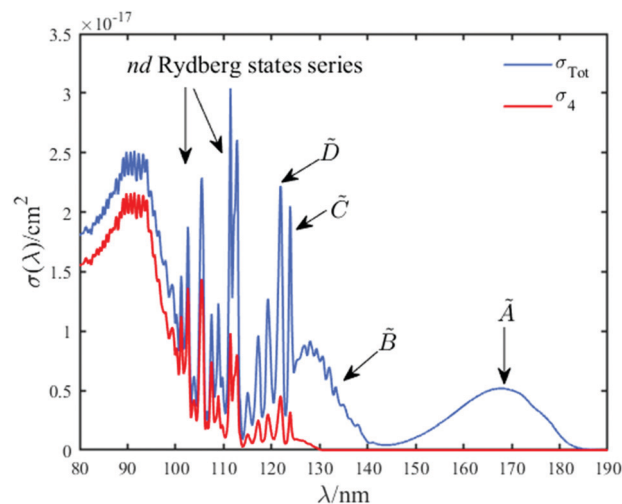**Fig. 3** The experimentally measured cross sections for H_2O vapor at 298 K. The total absorption cross section (σ_{tot}) and the three body partial cross section (σ_4) are plotted *versus* wavelength in nm. The presumed absorption bands are labeled by the upper state of the excitation.

A. Time dependent modeling, comets

As a simple model for the photochemistry of cometary comae, we consider a low-temperature, low-pressure gas irradiated for finite time with a standard air mass zero solar spectrum corresponding the light intensity at 1 AU, *i.e.* the 2000 ASTM Standard Extraterrestrial Spectrum Reference E-490-00.[29] The parameters for the modeling are selected to roughly model the coma of the 67P/Churyumov-Gerasimenko comet recently observed by the Rosetta spacecraft.[30] Hence the temperature was chosen to be 180 K, the pressure 2.5×10^{-5} Pa, and gas mixture of $0.56:0.33:0.11$ of $H_2O:CO_2:CO$. The spacecraft observed the presence of molecular dioxygen (O_2) that was correlated to that of H_2O suggesting the possibility that O_2 may be the descendant of the H_2O precursor species. While the conditions chosen were inspired by the 67P/C-G observations, they are not meant to represent a full simulation. Indeed, the chemistry of the comet and its coma is complex despite the relative simplicity of the reagents.[31,32] The solar spectrum can induce solid phase radiolysis of the nucleus which is not modeled here. Once gases are dispelled into the coma, the radiation can induce photochemistry in the parent or daughter species. The photochemistry of the primary secondary products as well as the subsequent reaction kinetics is explicitly modeled. The VUV radiation present in the spectrum can result in significant degrees of molecular ionization in the coma which is also not modeled. The coma is generated by sublimation through solar heating and disperses in a finite time according to hydro-dynamic flow. Hence, unlike atmospheric models, the chemistry is modeled for finite times and is not in steady state. It is possible that inhomogeneous grain chemistry may contribute, which we have investigated using the method developed by Herbst and coworkers.[33] The gas density falls off rapidly away from the Knutson Layer, and the probability of termolecular chemistry becomes very small. For the most part, therefore, the gas phase chemistry is driven by photochemistry and the subsequent unimolecular, bimolecular, and surface chemical reactions.

The most basic modeling scenario is provided by a batch, or plug flow, reactor. In this scheme, the gas mixture is irradiated at constant temperature and pressure for a finite period of time which is related to distance by the flow rate. The generation of ionic species is neglected by assuming the available light is limited in the ionization regions of the spectrum. A model consisting of 324 reversible neutral gas phase reactions, 31 grain catalyzed reactions, and the full photochemistry of primary and secondary products was initially considered. These comprise a comprehensive compilation of the possible neutral processes induced by the photolysis of the $H_2O/CO_2/CO$ species, as well as the photochemistry of the daughter molecules and grain catalyzed products. The gas phase chemical model was implemented using the Cantera package,[33] while the grain chemistry was modeled using the method of Herbst and coworkers employing a grain number density of 10^8 molecule per m^3 with grains of radii ~ 1000 Å.[34] Most of the reactions were found to be of negligible importance due to the low temperatures and pressures. The most important chemical processes are listed in Table 1 along with the associated rates.

B. Planetary atmospheres

Another important application of photochemical modeling is provided by the treatment of planetary atmospheres. These environments require quite different modeling conditions from those appropriate for interstellar molecular clouds or comet comae. In addition to the distinct temperature, pressure, and chemical compositions involved, the atmospheric photochemical kinetics are strongly affected by atmospheric transport, terrestrial sources and sinks, and solar shielding. Because of these factors, the relative significance of various photodissociation processes in the overall chemistry tend to be strong functions of altitude with the VUV induced chemistry occurring mostly at high altitudes. Moreover, in contrast to cometary environments, the observed atmospheric abundances are the result of a steady state condition achieved over very long timescales.

To assess the role of the new photodissociation cross-sections, we used the 1D atmospheric photochemistry model of Hu *et al.*,[28] designed for flexible exploration of photochemical parameter space. This model encodes 111 CHNOS chemical species linked by 900 unimolecular, bimolecular, termolecular, and photochemical steps that occur, of which a subset can be employed to simulate a given photochemical scenario. The chemical model is coupled at the boundaries with terms for terrestrial sources and sinks (oceans, volcanos, *etc.*), and for planetary escape (H_2, H). The physical transport is governed by a one-dimensional continuity-transport equation which treats the vertical flux for each species *via* eddy diffusion and molecular diffusion. The photolysis rates are computed using an actinic flux that includes the influence of Rayleigh scattering from gases and Mie scattering from S_8 and H_2SO_4 aerosols. The resulting time and space-dependent kinetic equations are expressed on a vertical spatial grid and solved using a stable time integrator. The propagation is continued until a steady-state is established.

9238 | *Phys. Chem. Chem. Phys.*, 2021, **23**, 9235–9248

This journal is © the Owner Societies 2021

Table 1 Reaction labeling and rate coefficients[a]

Neutral gas phase chemical reactions

Index	Reaction[a]	Rate coefficient[b] $k = AT^n e^{-\frac{E_a}{RT}}$
R1	$H_2 + O \rightleftharpoons H + OH$	$3.87 \times 10^4 T^{2.7} e^{-\frac{26200}{RT}}$
R2	$HCO + O \rightleftharpoons CO + OH$	3.00×10^{13}
R3	$HCO + O \rightleftharpoons CO_2 + H$	3.00×10^{13}
R4	$H + O_2 + M \rightleftharpoons HO_2 + M$	$2.80 \times 10^{18} T^{-0.86}$ (collision efficiency: CO: 0.75, CO_2: 1.5, H_2O: 0, O_2: 0)
R5	$H + 2O_2 \rightleftharpoons HO_2 + O_2$	$6.50 \times 10^{18} T^{-1} e^{-\frac{26200}{RT}}$
R6	$H + H_2O + O_2 \rightleftharpoons H_2O + HO_2$	2.32×10^{17}
R7	$H + O_2 \rightleftharpoons O + OH$	$2.65 \times 10^{16} T^{-0.67} e^{-\frac{71300}{RT}}$
R8	$2H + H_2O \rightleftharpoons H_2 + H_2O$	1.00×10^{17}
R9	$H + HO_2 \rightleftharpoons H_2O + O$	$3.97 \times 10^{12} e^{-\frac{2810}{RT}}$
R10	$H + HO_2 \rightleftharpoons H_2 + O_2$	$4.48 \times 10^{13} e^{-\frac{4470}{RT}}$
R11	$H + HO_2 \rightleftharpoons 2OH$	$8.4 \times 10^{13} e^{-\frac{2660}{RT}}$
R12	$H + HCO + M \rightleftharpoons CH_2O + M$	$2.47 \times 10^{24} T^{-2.57} e^{-\frac{1780}{RT}}$ (collision efficiency: CH_4: 2, CO: 1.5, CO_2: 2, H_2: 2, H_2O: 6)
R13	$H + HCO \rightleftharpoons CO + H_2$	7.34×10^{13}
R14	$2OH + M \rightleftharpoons H_2O_2 + M$	$2.30 \times 10^{18} T^{-0.9} e^{-\frac{7110}{RT}}$ (collision efficiency: CH_4: 2, CO: 1.5, CO_2: 2, H_2: 2, H_2O: 6)
R15	$2OH \rightleftharpoons H_2O + O$	$3.57 \times 10^4 T^{2.4} e^{\frac{8830}{RT}}$
R16	$HO_2 + OH \rightleftharpoons H_2O + O_2$	$1.45 \times 10^{13} e^{\frac{2100}{RT}}$
R17	$H_2O_2 + OH \rightleftharpoons H_2O + HO_2$	$2.00 \times 10^{12} e^{-\frac{1790}{RT}}$
R18	$O + O_2 + M \rightleftharpoons O_3 + M$	2.18×10^{14}
R19	$CO + OH \rightleftharpoons CO_2 + H$	$4.76 \times 10^7 T^{1.3} e^{-\frac{292}{RT}}$
R20	$HCO + OH \rightleftharpoons CO + H_2O$	5.00×10^{13}
R21	$CH + H_2 \rightleftharpoons CH_2 + H$	$1.08 \times 10^{14} e^{-\frac{13000}{RT}}$
R22	$H_2O + HCO \rightleftharpoons CO + H + H_2O$	$1.50 \times 10^{18} T^{-1} e^{-\frac{71100}{RT}}$

Photodissociation reactions

Index	Reaction	J value/s^{-1}
R23	$H_2O + h\nu \rightarrow H + OH$	9.74×10^{-6}
R24	$H_2O + h\nu \rightarrow H + H + O$	1.14×10^{-6}
R25	$CO_2 + h\nu \rightarrow CO + O$	1.59×10^{-7}
R26	$H_2O_2 + h\nu \rightarrow 2OH$	1.06×10^{-4}
R27	$H_2O_2 + h\nu \rightarrow H + HO_2$	4.20×10^{-6}
R28	$HO_2 + h\nu \rightarrow O + OH$	5.88×10^{-4}

[a] Backward reactions, where the right-hand side is the reagent, are denoted with an * in the text. [b] The units of rate coefficient is cm^3 mol^{-1} s^{-1} for 2nd order reactions and cm^6 mol^{-2} s^{-1} for 3rd order reactions. The activation energies are given in cal mol^{-1}.

This yields a set of concentration profiles as functions of altitude. The model has been validated using modern Earth and modern Mars as test cases, has recently been intercompared with other photochemical models in the regime of early Earth-like planets, and has been updated with newly measured NUV (200–230 nm) cross-sections[35] In the present simulations, we merely substitute the newly observed H_2O photodissociation cross-sections for the earlier literature data presently incorporated into the model.

In this report, we consider three modeling scenarios corresponding to modern Earth, modern Mars, and a CO_2 dominated benchmark scenario of Hu et al.,[28] which we take as representative of an early Earthlike planet. The detailed data sets are discussed elsewhere, but here we briefly note their characteristics. (1) The modern Earth model uses initial parameters consistent with contemporary conditions, i.e. nominal mixing ratios of 0.8 N_2, 0.2 O_2 and 350 ppmv of CO_2 with a water vapor mixing ratio at the surface of 0.01. The VUV radiation is highly screened by the atmosphere so the photochemistry of interest here can only occur at very high altitudes. The amount of available water vapor also decreases with altitude, so that in the mesosphere we have mixing ratios less than 10^{-5}. (2) Modern Mars has a CO_2/N_2 dominated atmosphere with surface mixing ratios of 0.95/0.026 and smaller amounts of CO, O_2, and H_2O with surface mixing ratios of roughly 1.7×10^{-3}, 7.5×10^{-4}, and 3.0×10^{-4}. The atmosphere is thin, with a surface pressure of 610 Pa and a mean temperature of 215 K. The water vapor decreases with altitude so that in the upper photolytic regions the mixing ratio of water is on the order of 10^{-7}. (3) The potential early (prebiotic) Earth scenario, $\sim$3.8 Ga, is a nearly oxygen devoid, and CO_2 and water rich planetary environment. The surface temperature is 288 K, and surface mixing ratios of 0.9, 0.1, and 0.01 for CO_2, N_2 and H_2O respectively fall into the broad range allowed by geochemical and modeling constraints[36] with the solar spectrum corresponding to the young Sun.[36] Our photochemical network omits hydrocarbon haze formation and nitrogenous chemistry following reasoning in Hu et al. 2012.[34] As sensitivity tests, we also consider the N_2- and H_2-dominated benchmark scenarios of Hu et al. 2012,[28] spanning a wide range of atmospheric redox state, and irradiation by the modern Sun instead of the young Sun. Our broad conclusions are robust to these sensitivity tests.

III. Results

A. Finite time simulations: comet model

Using the plug flow scheme outlined above, the chemical evolution from various initial conditions were propagated for times up to 10^7 s, which is considerably longer than is realistically required for a cometary model. To provide an overview of the chemistry, a typical kinetic trajectory profile is shown in Fig. 4a, which corresponds to the 67P/C-G condition. In Fig. 4b the production rates of H, O, OH are shown along with the rates are various important reaction steps. In Fig. 4c, the production rates of various daughter species are shown along with the rates of the key associated reaction steps. These results are generated including all photochemical reactions, secondary reactions and grain chemistry. (However, again, this is a simplistic model that ignores ionization, radiolysis, and complex hydrodynamics with the aim of assessing the rough level of impact of the H_2O photodissociation channels.) It is seen initially that the concentrations of primary photochemical radical products X = H, OH, and O, each grow linearly with time, i.e. [X] $\sim$ $t^{1.0}$ due to the photolysis of H_2O and CO_2. The primary daughter species (Y) are HO_2, H_2O_2, H_2, and O_2 which are the result of molecular collisions that occur roughly on a time scale $\sim$1 s. The production of O_2, H_2, and H_2O_2 are found to proceed as [Y] $\sim$ $t^{3.0}$ as would be consistent with a radical–radical
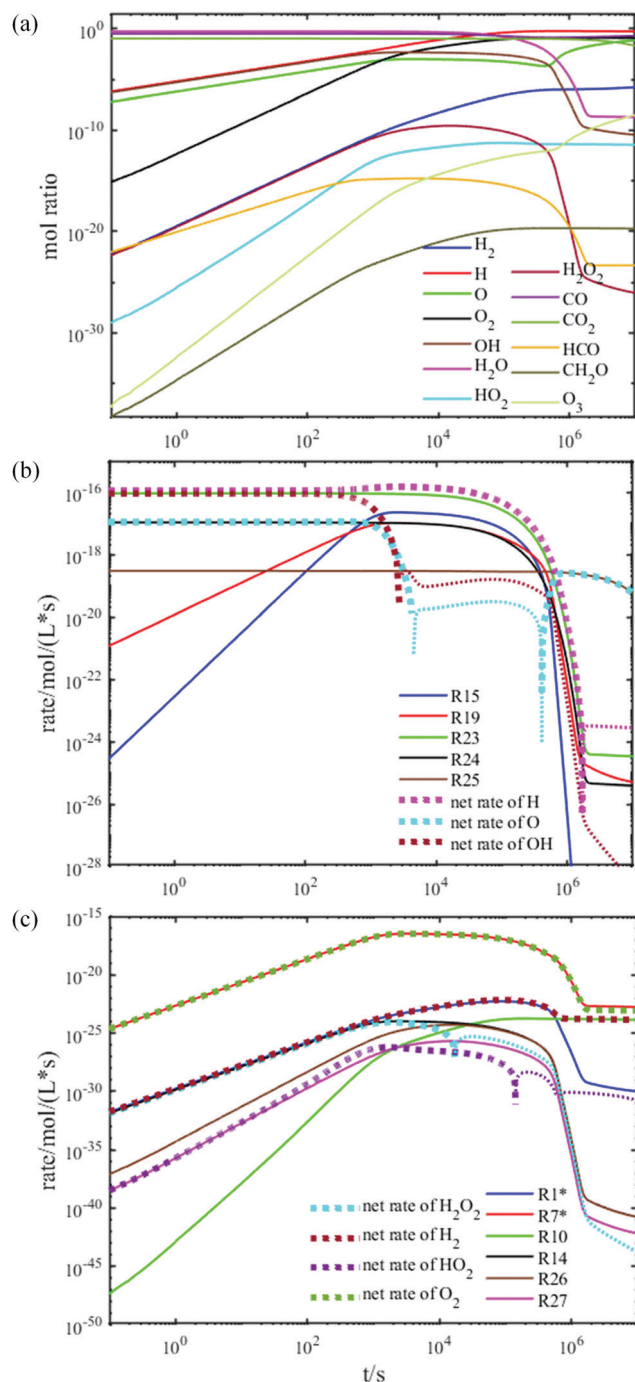
Fig. 4 The kinetic trajectory computed for the 67P/C-G simulation. In (a) the concentrations (as a mol ratio) *vs.* time for all significant species. In (b) the rates (M s^{-1}) of the important primary reaction steps and formation rates of primary products. In (c) the rates of important reaction steps along with the formation rates of various product species. In (b) and (c) the dotted lines are the total species production rates and solid lines are reaction step rates. The transition from thick to thin dotted lines shows the transition to negative species rates.

binary mechanism, *i.e.* rate $\sim [\mathrm{X}]^2$ although the concentrations are tiny due to the low pressure. On the other hand, $[\mathrm{HO_2}]$ proceeds as $[\mathrm{HO_2}] \sim t^{4.0}$ before $t = 10$ s, and then becomes $[\mathrm{HO_2}] \sim t^{4.4}$ at $t = 10$–1000 s, suggesting a more complicated

production mechanism. From Fig. 4b it is seen that for the "early" kinetics the primary source of H_2 is $H + OH \rightarrow H_2 + O$ (R1*), of O_2 is $O + OH \rightarrow O_2 + H$ (R7*), of H_2O_2 is $OH + OH + M \rightarrow H_2O_2 + M$ (R14), and of HO_2 is $H_2O_2 + h\nu \rightarrow HO_2 + H$ (R27). The R* notation indicates the reverse reaction in Table 1. With the exception of the HO_2 product, a simple one step production mechanisms thus account for the trivial chemistry during the initial phase of the chemistry. The HO_2 production requires us also to include several HO_2 sink reactions. The grain chemistry is found to have a negligible impact on the chemistry of any of the important primary or secondary products. Even though the collision time of radicals with solid particles is on the order of 100–1000 s, the subsequent desorption rates from the grain surface are high enough so that there is little net accommodation from the gas phase. Only for the minor products, HCO and H_2CO, do we see a significant effect, which are enhanced by surface recombination.

At approximately 500–1000 s it is seen that the behavior of the trajectory begins to deviate from the simple kinetics seen in the initial phase of direct photolysis, thus signaling new chemistry. The net production rate of OH and O radicals falls by over two orders of magnitude as these radicals go into an approximate steady state that occurs when the chemical processing of the photochemical product radicals becomes important. Most importantly, the rates increase for the reactions, $CO + OH \rightarrow CO_2 + H$ (R19), $OH + OH \rightarrow H_2O + H$ (R15), and $OH + O \rightarrow O_2 + H$ (R7*), all of which significantly compensates the photochemical production. The reaction $OH + O \rightarrow O_2 + H$ (R7*) is the primary sink for O and source for O_2. In the steady state region, the rate of reaction $CO + OH \rightarrow CO_2 + H$ (R19) plateaus since the reagent concentrations are roughly constant. On the other hand, the net production rate for the H-radical actually increases at about $t \sim 1000$ s since it is a byproduct of the reactions $CO + OH \rightarrow CO_2 + H$ (R19) and $O + OH \rightarrow O_2 + H$ (R7*). The H-atom builds to high concentrations, which presumably would show a high degree of diffusive escape in a realistic transport model. The primary chemical source of O_2 remains $O + OH \rightarrow O_2 + H$ (R7*) throughout the course of the reaction. The variations of growth rate of O_2 concentration can be traced to sources and sinks for the reagent species O and OH. Similarly, the growth of H_2 at all time is accounted for by the $H + OH \rightarrow H_2 + O$ (R1*) process. However, the net production rate of H_2O_2 deviates from its primary source reaction $OH + OH + M \rightarrow H_2O_2 + M$ (R14) as the photodissociation of H_2O_2, $H_2O_2 + h\nu \rightarrow 2OH$ (R26) became significant which is the sink of H_2O_2.

At ~ 2000 s–10^5 s, O and OH radical stay roughly at steady state and the O_2 concentration grows linearly at this period. Since $d[O_2]/dt \approx k_{7*}[OH][O]$, the linear growth rate is reasonable. The net production rate of H_2 is seen to grow linearly before 10^4 s and then the production curve splits from its primary source as the contribution of reaction $H + HO_2 \rightarrow H_2 + O_2$ (R10) grows. Similarly, the behavior of H_2O_2 is dominated by reaction $OH + OH + M \rightarrow H_2O_2 + M$ (R14) before 10^4 s and thereafter by $H_2O_2 + h\nu \rightarrow 2OH$ (R26). After 10^5 s, chemical processes slow appreciably due to the depletion of H_2O reagent. As a result, there
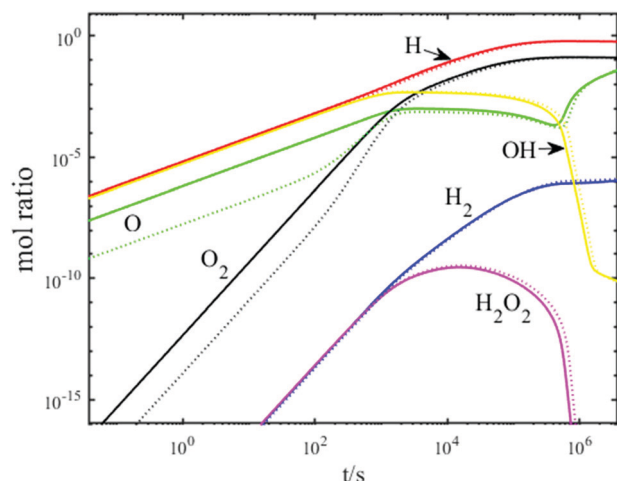
Fig. 5 The influence of the updated H_2O cross sections on the kinetic trajectory originally described in Fig. 4. The concentration *versus* time for several species using the old cross sections are plotted with dotted lines while those obtained with the new cross sections are plotted with solid lines. The O_2 concentration is substantially enhanced at early times, but becomes much closer to the original prediction for times $t > 1000$ s.

Fig. 6 The ratio of O_2 concentration *versus* time obtained using the new H_2O cross sections to those obtained with the original values in the kinetic trajectory of Fig. 4. The inset shows the long time behavior of the ratio.

is no further production of O_2 whose concentration peaks near 10^5 s at 9.3% of the mole fraction. It is expected that the true O_2 production within a coma will terminate before this end stage due to hydrodynamic flow.

To assess the role of the enhanced three body dissociation channel for H_2O, we first simply directly compare the kinetic trajectory to that generated using the conventional H_2O cross sections in the J-values. There are two common modeling scenarios. In one, the three body channel is totally neglected and so neutral photodissociation is assumed to proceed through the binary channel 1 *via* the full cross section σ_{tot}. In another, the branching ratios measured at the Lyman-α line is switched-on at small wavelengths. Since both schemes underestimate the true three body contribution, for simplicity we adopt a comparison to the first method, although we found both methods yield qualitatively similar behavior. In Fig. 5 we show the concentrations *versus* time where the new predictions
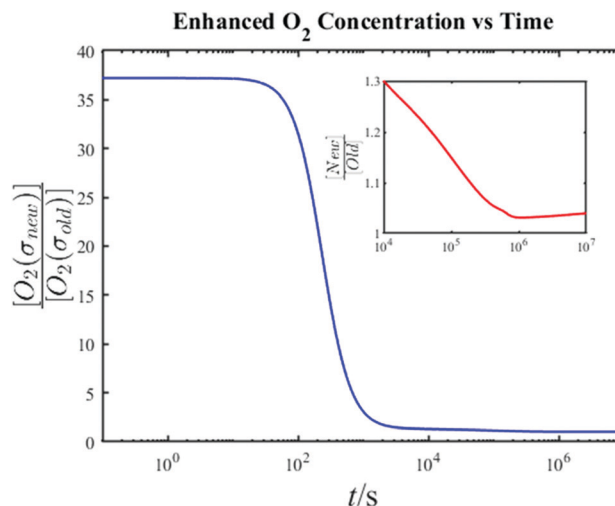
are plotted with solid lines and original results with dashed lines. At the short times, clear differences are apparent where the O and O_2 concentrations are roughly 36 times higher, although still small in absolute terms. Since the original O-production, and hence the O_2 production, is due to CO_2 photolysis, the difference of 36 reflects a difference in J-values of 7.2 and a difference in concentrations of 5.0, *i.e.* $\dfrac{J_{24}}{J_{25}} \cdot \dfrac{[H_2O]}{[CO_2]} = 7.2 \times 5.0 = 36$. At times in range 100–1000 s the modeling predictions become much closer and the concentration differences diminish to about 10%. As emphasized in Table 2, the long-time effect of the three body channel becomes small. This point is made more clearly in Fig. 6 where the ratio of O_2 concentrations obtained with the new and old cross sections are plotted *versus* time. As discussed above in connection with Fig. 4, the kinetics in this time window are characterized by the onset of bimolecular chemistry involving the photochemical radicals. In particular, the net production of O-atoms is greatly reduced as the chemical sink $O + OH \rightarrow O_2 + H$ (R7*) achieves balance with the photochemical production.

Table 2 The mol ratio computed using the new and old cross sections computed at two long times in the simulation

| Species[a]	Mol ratio at $t = 100\,000$ s			Mol ratio at $t = 10\,000\,000$ s		
	σ_{new}	σ_{old}	Difference (%)	σ_{new}	σ_{old}	Difference (%)
H_2	2.26×10^{-7}	2.23×10^{-7}	1.7	1.76×10^{-6}	1.75×10^{-6}	0.8
H	4.33×10^{-1}	3.94×10^{-1}	9.0	5.73×10^{-1}	5.72×10^{-1}	0.2
O	5.87×10^{-4}	4.74×10^{-4}	19.2	7.36×10^{-2}	7.99×10^{-2}	−8.6
O_2	9.32×10^{-2}	8.10×10^{-2}	13.1	1.24×10^{-1}	1.20×10^{-1}	3.8
OH	2.67×10^{-3}	3.15×10^{-3}	−18.1	3.70×10^{-11}	3.28×10^{-11}	11.2
H_2O	1.65×10^{-1}	2.01×10^{-1}	−22.0	2.03×10^{-9}	2.20×10^{-9}	−8.5
HO_2	5.83×10^{-7}	5.62×10^{-12}	100.0	3.79×10^{-12}	3.65×10^{-12}	3.7
H_2O_2	7.83×10^{-11}	1.14×10^{-10}	−45.1	9.47×10^{-27}	7.47×10^{-27}	21.1
CO	2.01×10^{-1}	2.07×10^{-1}	−3.0	2.08×10^{-1}	2.05×10^{-1}	1.4
CO_2	1.05×10^{-1}	1.13×10^{-1}	−7.6	2.15×10^{-2}	2.39×10^{-2}	−11.6
O_3	2.28×10^{-13}	1.50×10^{-13}	34.0	3.30×10^{-9}	3.40×10^{-9}	−2.9

[a] Major species.
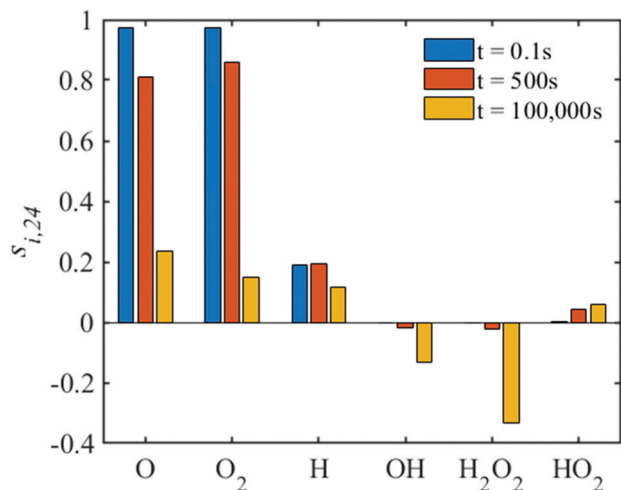
Fig. 7 The sensitivity indices for several species computed for the 67P/C-G trajectory at early, middle, and late times. The influence of the three body photodissociation channel is seen to diminish with increasing time for O_2 but becomes an increasing negative influence on H_2O_2.

The key feature of the new cross section is the increased O-atom production (along with that of H-atoms). How these modifications propagate through the chemical network is an interesting question which we explore using a chemical sensitivity analysis. We adopt a simple local sensitivity analysis where the response of a target observable with respect to multiple variable factors in the mechanism are carried out independently and assuming a linear response. The target functions are chosen to be the species concentration at a specific time t, $X_i(t)$, and the variable factors are taken to be the pre-exponential factor of the rate coefficients, k_j. We assume all the initial conditions of the trajectory remain fixed. The higher order correlations involved in a global analysis are unnecessary in this case.[37–39] We define a dimensionless local sensitivity index as

$$s_{i,j} = \frac{\partial \ln X_i(t)}{\partial \ln k_j}\bigg|_{k_j=k_0}$$

where k_0 are the model values of the rate coefficients. We note that the reverse rate coefficients are computed via the equilibrium constant and therefore their sensitivity coefficients are the negative of the forward coefficients, i.e., $s_{i,j^*} = -s_{i,j}$.

The results of the sensitivity analysis are shown in Fig. 7–9. In Fig. 7, we show the sensitivity $s_{i,24}$ of a number of species, O_2, O, H, OH, and H_2O_2 with respect to k_{24} that governs the three body process. The sensitivity indices for these species are shown for early, intermediate, and late times, i.e. 0.1 s, 500 s, and 10^5 s. The three body process is seen to have a strong effect on various species concentrations which tends to diminish with time. In Fig. 8, the most important $s_{i,j}$ are shown for six species computed at the fixed time, $t = 10^5$ s. These results show sensitivities to both photochemical and non-photochemical processes. In a more focused view on the O_2 production, in Fig. 9 the sensitivity of $[O_2(t)]$ is shown for several rate coefficients that is plotted continuously versus time, i.e. $s_{O_2,j}(t)$. The

values of $s_{O_2,j}$ shown for the three times in Fig. 7 are seen to be consistent with those in Fig. 9, but the continuous time plot makes clear the rapid variation vs. t that illustrates the rapid drop off in certain production modes, such as R23.

It is seen that the O + OH → O_2 + H (R7) reaction, which is the primary chemical source of O_2 production, has a high index at early times but becomes rather small at later times indicating it is then no longer rate limiting. The O-source reactions R15, R24, R25 have large positive value of sensitivity indices for [O] and hence also for [O_2] since it is a reagent in R7*. Likewise, the OH source, H_2O + $h\nu$ → OH + H (R23), has a large positive $s_{O_2,23}$ value while the OH-sink reaction, CO + OH → CO_2 + H (R19) exhibits a negative value $s_{O_2,19}$. So, in general, the rule is that to get more O_2 we need to promote reaction R7* which in turn requires more O and OH reagents.

The generation of dioxygen at early times, $t < 10^2$ s, is controlled by the photochemical sources H_2O + $h\nu$ → (OH + H and H + H + O) (R23 and R24) and CO_2 → CO + O (R25) followed by the one step process OH + O → O_2 + H. The new water cross sections give high [O_2] values primarily because the J-value for R24 is higher than that for R25, i.e. H_2O photolysis is a better source of O-atoms than is CO_2 photolysis. However, the sensitivity analysis reveals that the chemical processing of O and OH at longer times then drives down the influence of R23 and R24 while R25 grows more important. This emphasizes the negative role of free hydrogen in O_2 formation. In particular, the radicals H, O, and OH tend toward recombining to H_2O via reactions R19, R15, and R1. This trend would accelerate for higher pressures when the H-atom mole fraction is much lower due to recombination effects, such as H + H + M → H_2 + M, and the reaction OH + H_2 → H_2O + H, that are unimportant in the $p \sim 10^{-5}$ Pa range. We expect that at even lower pressures the recombination rate on grain surfaces will become a major sink for the photochemical radicals.

B. Planetary atmospheres

The exoplanet atmospheric model of Hu et al.[28] was applied to the three scenarios noted above, modern Earth, modern Mars, and early Earth. The original modeling is in ref. 28 and 40 where the detailed parameter settings are given. The present calculations retain those parameters except to update the H_2O photodissociation cross sections. Unlike the plug flow simulations discussed above, the observed steady-state concentrations in the atmospheric applications suppress the transient behavior and reflect a long time balance between the photochemical and transport processes. As a result, we find a much lower level of sensitivity to the details of the photochemical rates.

Consider first the modern Earth scenario. Since Earth's atmospheric O_2 levels are of biological origin, we focus on how the photolysis of H_2O influences the concentration of trace species containing the O-atom. In Fig. 10, the concentration of nine species are plotted versus altitude, OH, HO_2, NO, NO_2, N_2O, $HNO_3 \cdot H_2O$, O_3, and the greenhouse gas CH_4. The updated cross sections produce the results shown with dashed lines while the original results are given with the solid lines. Some very small differences between the predictions are seen at the
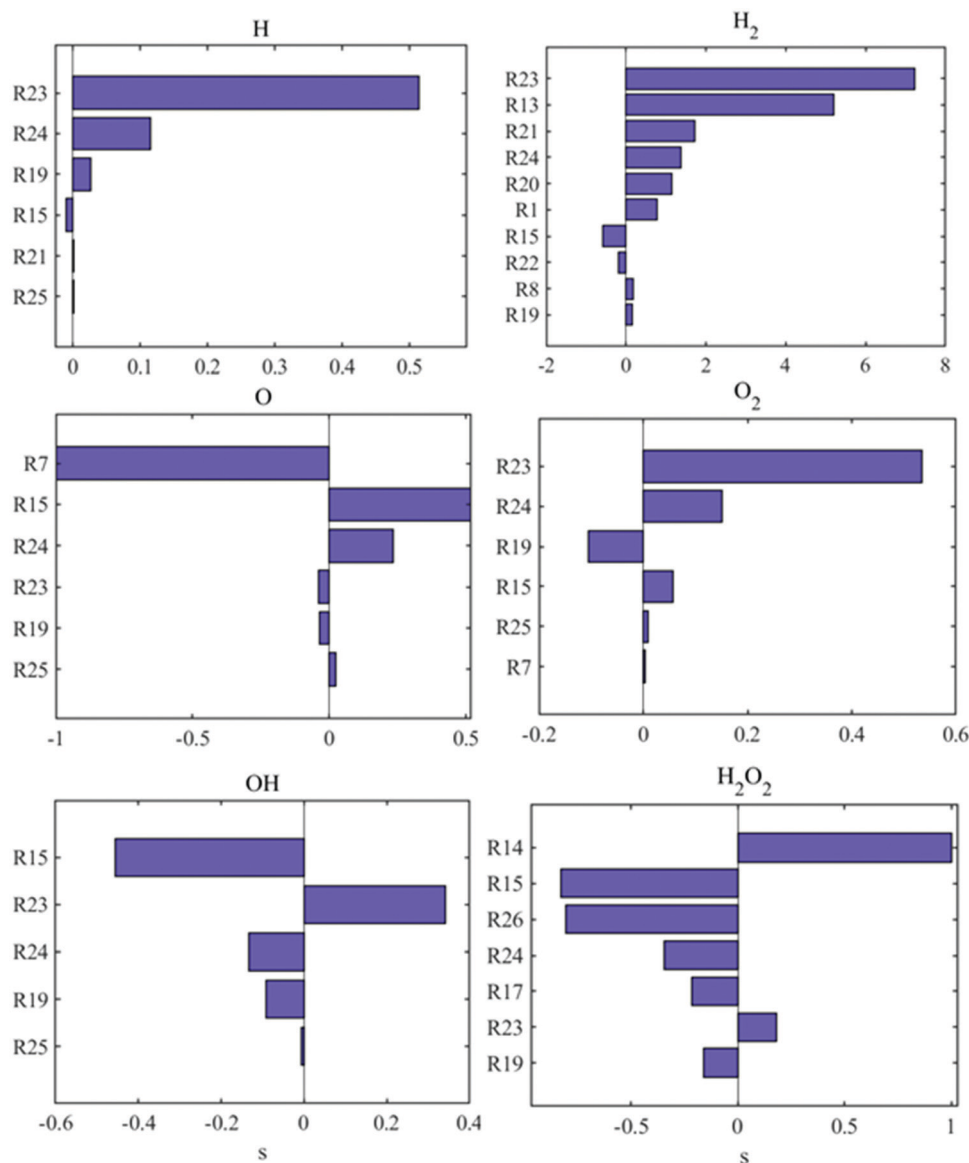
9242 | Phys. Chem. Chem. Phys., 2021, **23**, 9235–9248

This journal is © the Owner Societies 2021

Fig. 8 The sensitivity indices of various species computed at the time $t = 10^5$ s. The positive value for s_{ij} reflects a net increase in concentration of [i] due to an increase in k_j while a negative value indicates a decrease in [i].

highest altitudes, on the order of several percent. The screening of the solar radiation by atmospheric gases effectively limits the available VUV light to very low levels except at extremely high altitudes where there exist very few water molecules to potentially photolyze. The bulk composition of the atmosphere is thus effectively unchanged by the three body photodissociation process.

In Fig. 11, we present the results obtained using the conditions appropriate to present day Mars. The concentrations of most prevalent species (omitting the dominant CO_2 and N_2 species) are shown up to very high altitudes, $i.e.$ 120 km. The original results are shown with solid lines while the updated results are given by dashed lines. The O_2 species is of abiotic origin and its concentration is shown to have little dependence on altitude. Although the atmosphere is relatively thin, we see

very little influence of the three body channel on the equilibrium concentrations on any of the species. The photochemical processes occurring at longer wavelengths, in particular $CO_2 + h\nu \rightarrow CO + O$ and $H_2O + h\nu \rightarrow OH + H$, dominate the photochemistry and the three body channel has relatively little influence. Again, this is a result of the low levels of UV light present for $\lambda < 130$ nm compared with that for 242 nm $> \lambda > 130$ nm.

Finally, in Fig. 12 we show the results $versus$ altitude for the CO_2 dominated early Earth scenario at the temperature 288 K. In this case there is no biological O_2 present, and there are fairly abundant levels of surface water. The updated and original results are shown with dashed and solid lines, respectively. The three body process is seen, again, to have relatively little effect on the [O_2] levels. We notice the [H_2O]
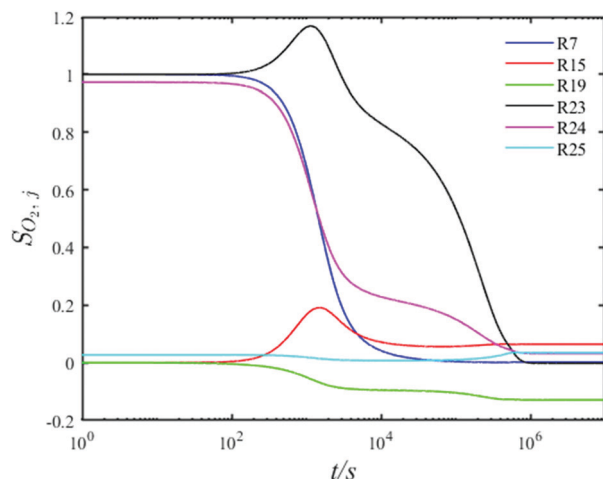
Fig. 9 The sensitivity indices for [O_2] at $t = 10^5$ s with respect to various rate coefficients. It is seen that at early and middle times the [O_2] is most sensitive to the H_2O photolysis rates (and the primary production step O + OH → O_2 + H (R7*)). At late times it is most sensitive to CO_2 photolysis and the three body photodissociation but the chemical steps R15 and R19 also play a large role.

profile *versus* altitude is seen to fall off by roughly 5–6 orders of magnitude within 15 km of sea level. Thus, relatively little H_2O is present at the higher altitudes where the VUV photolysis process can occur. Instead, the O_2 generation seems to be driven by CO_2 photodissociation as predicted by the conventional model (Fig. 13). The main difference between the two treatments is a slightly higher level of H_2O depletion at high altitudes, although the bulk composition of the atmosphere is largely unchanged. The results were similar under irradiation corresponding to the modern Sun (Fig. 14). In sensitivity tests to atmospheres of varying bulk composition, variation was also modest, with the largest variation for the N_2-dominated atmosphere. In this more transparent atmospheric scenario, VUV radiation penetrated deeper into the atmosphere producing higher rates of R24; in this scenario, we noted pH_2 to increase by 34%. In light of the uncertainties embedded into the model, we consider this negligible, which preserves our overall conclusion of insignificant variation due to inclusion of our new photochemical pathway.
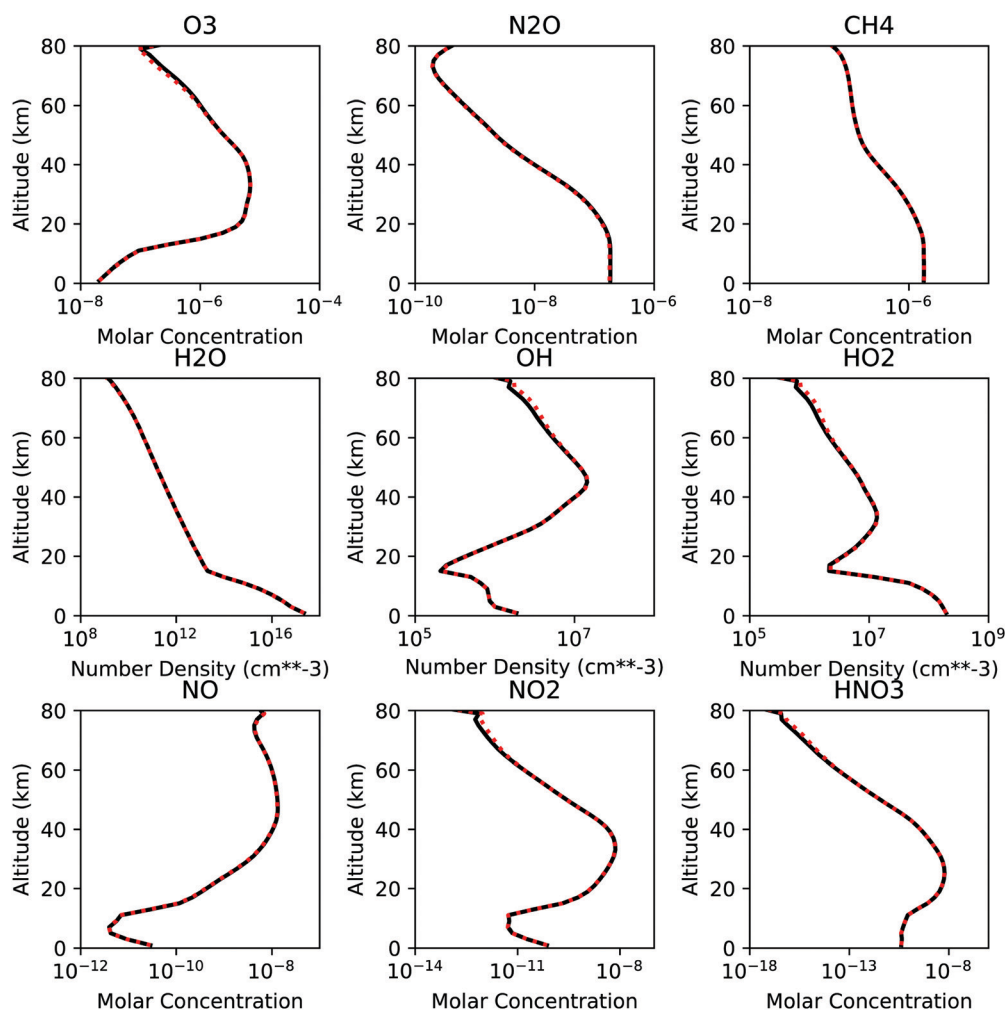

Fig. 10 The predicted concentration of nine minor species in the modern Earth atmosphere as a function of altitude. The solid lines are the result obtained using the original H_2O cross sections while the dashed lines are those obtained using the updated cross sections.
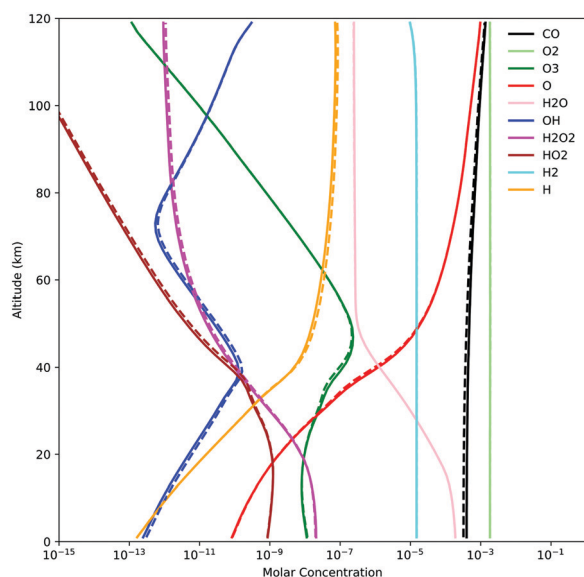
9244 | *Phys. Chem. Chem. Phys.*, 2021, **23**, 9235–9248

This journal is © the Owner Societies 2021

Fig. 11 The predicted concentrations for various atmospheric gases for modern Mars conditions. The results using updated H_2O cross sections are plotted using dashed lines while the original results are shown using solid lines. The differences are so small as to make the lines almost indistinguishable.
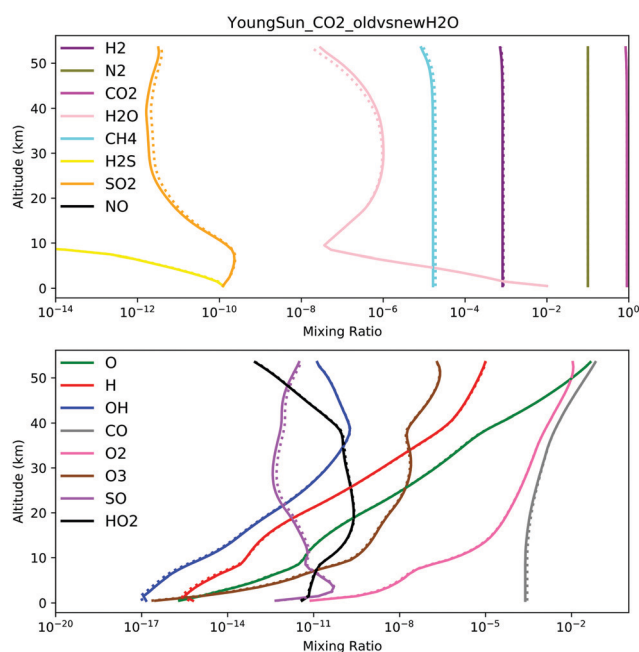

Fig. 12 Predicted concentrations *versus* altitude for a model corresponding to a representative early Earth-type atmosphere at 288 K dominated by CO_2 gas, corresponding to the CO_2-dominated benchmark scenario of Hu *et al.* 2012,[28] subject to irradiation by the 3.8 Ga sun.[37] The model predictions employing the updated H_2O photodissociation cross sections are shown with dashed lines while the conventional cross section results are shown with solid lines.

IV. Conclusion

The tunable VUV light source at the DCLS provides a unique opportunity to study photon-initiated chemistry in spectral
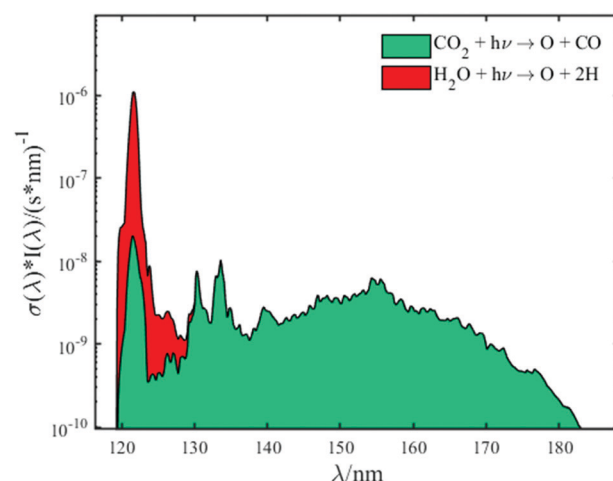

Fig. 13 Two photochemical sources of O-atoms. The product of the solar intensity and the photodissociation cross-section for the H_2O three body process, $H_2O + h\nu \rightarrow H + H + O$ (R24), and photodissociation of CO_2, $CO_2 + h\nu \rightarrow CO + O$ (R25). It is seen that the three body dissociation is the dominant source for O-atoms. The J-value for the $\sigma_4^{H_2O}$ is 1.14(−6) s^{-1} while the J-value for σ^{CO_2} is 1.59(−7) s^{-1}.
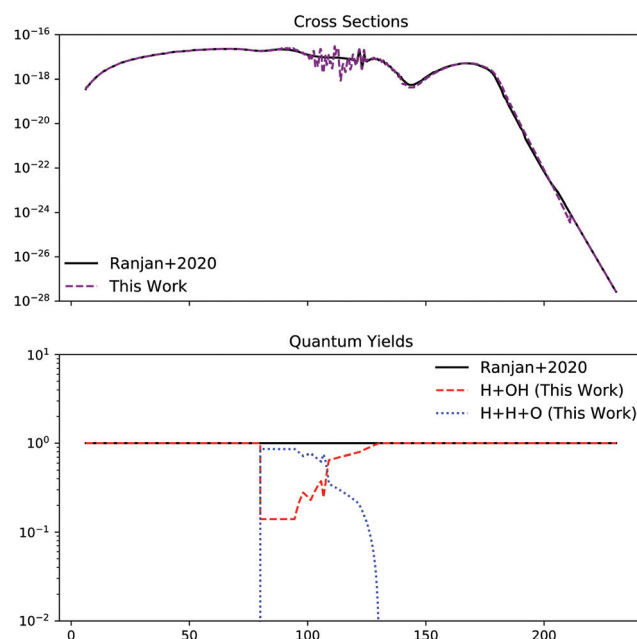

Fig. 14 Incorporation of new H_2O cross-sections and photodissociation pathway into terrestrial planet atmospheric photochemistry model.[28,36] Black curves represent H_2O photodissociation parameters formulated by Ranjan *et al.* 2020[36] (their "extrapolation" prescription), and represent the control. Colored lines represent H_2O photodissociation parameters derived by incorporating the results of this work.

regimes that were previously inaccessible. When combined with a high accuracy product detection scheme, the quantum yields for high energy dissociation channels of gas phase molecules can be probed as functions of wavelength. The quantum yield reflects dynamics occurring on the excited state potential energy surfaces and, for many molecules, will reveal the complexity of the nonadiabatic dynamics that follows the

initial excitation process. While theory can, in principle, provide quantum yields *versus* energy, the calculations are difficult and an experimental determination is desirable. In this work, we have investigated some consequences of the newly observed H_2O photodissociation cross sections. Somewhat unexpectedly, the three body dissociation channel, $H_2O + h\nu \rightarrow O + H + H$, was found to be of increasingly high importance at wavelengths below the Lyman-α line at 121.6 nm. Since the photodissociation of water is a fundamental process of great importance in modeling the behavior of many systems of astrophysical significance, it is useful to consider the implications of this new result in practical circumstances.

When water vapor is exposed to solar radiation, it is generally assumed that the dominant photochemical channel is H + OH. The generation of O-atoms *via* the three body breakup channel $H_2O + h\nu \rightarrow O + H + H$ is energetically forbidden for wavelengths above 130 nm and is often ignored in photochemical modeling. It is often presumed that the photolysis of CO_2 is the chief source of O-atoms in applications since it can occur at wavelengths up to 227 nm. For atmospherically screened light this seems quite reasonable since the VUV radiation necessary for the three body channel is largely eliminated from the spectrum (Fig. 15). However, as shown in, when exposed to unscreened solar radiation the $H_2O + h\nu \rightarrow O + H + H$ process actually outstrips $CO_2 + h\nu \rightarrow O + CO$ by a factor of 7.2. In Fig. 13, the density $\sigma_j(\lambda) \cdot I(\lambda)$ is plotted which shows a large contribution to the H_2O quantum yield near and below the Lyman-α line. Of course, the photolysis of water also produces two H-atoms that can also influence the subsequent chemistry. Thus, detailed chemical modeling is required to establish the net significance of the process.

Of particular consequence in applications is the possibility of generating molecule oxygen, *i.e.* O_2 from O-atoms. We considered in this work two general environments, the atmospheres of planets exposed to solar radiation, and the extremely diffuse atmospheres (comae) of comets. The coma of a comet is particularly interesting application for the update since the coma is usually dominated by

water vapor and effects of light screening are minimal. We have found that inclusion of the updated H_2O cross sections had a large effect on the O_2 production rate at short times following sublimation, corresponding to gas concentrations occurring at relatively short distances from the comet nucleus. The dominant chemical source of O_2 in this environment is $O + OH \rightarrow O_2 + H$ since recombination *via* $O + O + M$ is improbable at these low pressures. At longer times, and hence longer distances from the nucleus, the O_2 concentration reverted to values near the predictions that ignore the three body channel. After a sensitivity analysis it was found that the chemical processing of the O + H + H three body products tended to cancel the effects of this channel for the creation of O_2 at these longer times. However, the outward hydrodynamic flux and expansion of the gas effectively limits the time over which molecular collisions can occur.

The applications to planetary atmospheres largely concluded that there was little effect of the three body channel on the bulk chemical compositions. The atmospheric screening of VUV radiation restricts the new chemistry to the highest altitudes where there is generally little water vapor. Furthermore, due to chemical equilibration, the production of O-atoms is compensated by a sequence of reactions that tend to result in H_2O recombination or the formation of other reduced compounds rather than forming O_2.

Conflicts of interest

There are no conflicts to declare.

Acknowledgements

References

1. K. Yuan, R. N. Dixon and X. Yang, Photochemistry of the water molecule: Adiabatic versus nonadiabatic dynamics, *Acc. Chem. Res.*, 2011, **44**, 369–378.
2. S. A. Harich, D. W. H. Hwang, X. Yang, J. J. Lin, X. Yang and R. N. Dixon, Photodissociation of H_2O at 121.6 nm: A state-to-state dynamical picture, *J. Chem. Phys.*, 2000, **113**, 10073–10090.
3. D. H. Mordaunt, M. N. R. Ashfold and R. N. Dixon, Dissociation dynamics of $H_2O(D_2O)$ following photoexcitation at the Lyman-α wavelength (121.6 nm), *J. Chem. Phys.*, 1994, **100**, 7360–7375.
4. R. Van Harrevelt and M. C. Van Hemert, Photodissociation of water. I. Electronic structure calculations for the excited states, *J. Chem. Phys.*, 2000, **112**, 5777–5786.
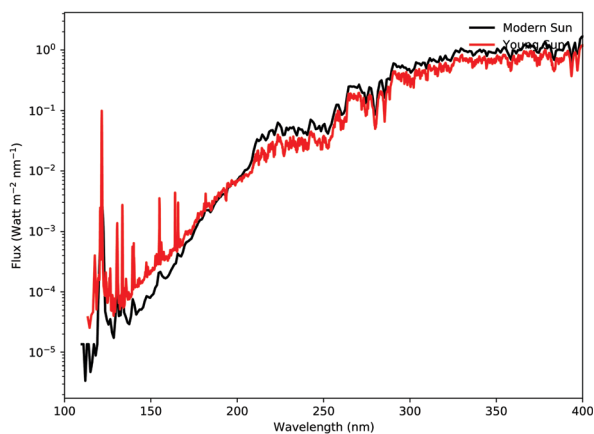
Fig. 15 Input stellar spectra used in terrestrial planet atmospheric photochemistry model. The black line corresponds to the modern Sun spectrum utilized by Hu *et al.* 2012.[28] The red line corresponds to a young Sun spectrum (3.8 Ga) draw from Claire *et al.* 2012.[37]

9246 | *Phys. Chem. Chem. Phys.*, 2021, **23**, 9235–9248

This journal is © the Owner Societies 2021

5 R. Van Harrevelt and M. C. Van Hemert, Photodissociation of water. II. Wave packet calculations for the photofragmentation of H$_2$O and D$_2$O in the B̃ band, *J. Chem. Phys.*, 2000, **112**, 5787–5808.

6 R. N. Dixon, D. W. Hwang, X. F. Yang, S. Harich, J. J. Lin and X. Yang, Chemical 'double silts': Dynamical interference of photodissociation pathways in water, *Science*, 1999, **285**, 1249–1253.

7 V. Engel, R. Schinke and V. Staemmler, Photodissociation dynamics of H$_2$O and D$_2$O in the first absorption band: A complete ab initio treatment, *J. Chem. Phys.*, 1988, **88**, 129–148.

8 M. Brouard, S. R. Langford and D. E. Manolopoulos, New trends in the state-to-state photodissociation dynamics of H$_2$O(Ã), *J. Chem. Phys.*, 1994, **101**, 7458–7467.

9 B. P. Bonev, M. J. Mumma, M. A. DiSanti, N. Dello Russo, K. Magee-Sauer, R. S. Ellis and D. P. Stark, A Comprehensive Study of Infrared OH Prompt Emission in Two Comets. I. Observations and Effective g-Factors, *Astrophys. J.*, 2006, **653**, 774–787.

10 E. F. Van Dishoeck, E. Herbst and D. A. Neufeld, Interstellar water chemistry: From laboratory to observations, *Chem. Rev.*, 2013, **113**, 9043–9085.

11 D. C. Catling and J. F. Kasting, *Atmospheric evolution on inhabited and lifeless worlds*, Cambridge University Press, 2017.

12 M. Nicolet, On the photodissociation of water vapour in the mesosphere, *Planet. Space Sci.*, 1984, **32**, 871–880.

13 D. R. Bates and M. Nicolet, The photochemistry of atmospheric water vapor, *J. Geophys. Res.*, 1950, **55**, 301–327.

14 J. E. Frederick and R. D. Hudson, Atmospheric Opacity. in the Schumann-Runge Bands and the Aeronomic Dissociation of Water Vapor, *J. Atmos. Sci.*, 1980, **37**, 1088–1098.

15 Y. Chang, Q. Li, F. An, Z. Luo, Y. Zhao, Y. Yu, Z. He, Z. Chen, L. Che, H. Ding, W. Zhang, G. Wu, X. Hu, D. Xie, J. M. C. Plane, W. Feng, C. M. Western, M. N. R. Ashfold, K. Yuan and X. Yang, Water Photolysis and Its Contributions to the Hydroxyl Dayglow Emissions in the Atmospheres of Earth and Mars, *J. Phys. Chem. Lett.*, 2020, **11**, 9086–9092.

16 R. Mota, R. Parafita, A. Giuliani, M. J. Hubin-Franskin, J. M. C. Lourenço, G. Garcia, S. V. Hoffmann, N. J. Mason, P. A. Ribeiro, M. Raposo and P. Limão-Vieira, Water VUV electronic state spectroscopy by synchrotron radiation, *Chem. Phys. Lett.*, 2005, **416**, 152–159.

17 C. Y. Chung, E. P. Chew, B. M. Cheng, M. Bahou and Y. P. Lee, Temperature dependence of absorption cross-section of H$_2$O, HOD, and D$_2$O in the spectral region 140-193 nm, *Nucl. Instrum. Methods Phys. Res., Sect. A*, 2001, **467–468**, 1572–1576.

18 L. C. Lee and M. Suto, Quantitative photoabsorption and fluorescence study of H$_2$O and D$_2$O at 50-190 nm, *Chem. Phys.*, 1986, **110**, 161–169.

19 T. G. Slanger and G. Black, Photodissociative channels at 1216 Å for H$_2$O, NH$_3$, and CH$_4$, *J. Chem. Phys.*, 1982, **77**, 2432–2437.

20 H. T. Wang, W. S. Felps and S. P. McGlynn, Molecular Rydberg states. VII. Water, *J. Chem. Phys.*, 1977, **67**, 2614–2628.

21 Y. Chang, S. Yu, Q. Li, Y. Yu, H. Wang, S. Su, Z. Chen, L. Che, X. Wang, W. Zhang, D. Dai, G. Wu, K. Yuan and X. Yang, Tunable VUV photochemistry using vacuum ultraviolet free electron laser combined with H-atom Rydberg tagging time-of-flight spectroscopy, *Rev. Sci. Instrum.*, 2018, **89**, 063113.

22 H. Wang, *et al.*, Photodissociation dynamics of H$_2$O at 111.5 nm by a vacuum ultraviolet free electron laser, *J. Chem. Phys.*, 2018, **148**, 124301.

23 Y. Chang, Y. Yu, H. Wang, X. Hu, Q. Li, J. Yang, S. Su, Z. He, Z. Chen, L. Che, X. Wang, W. Zhang, G. Wu, D. Xie, M. N. R. Ashfold, K. Yuan and X. Yang, Hydroxyl super rotors from vacuum ultraviolet photodissociation of water, *Nat. Commun.*, 2019, **10**, 1–7.

24 Y. Chang, F. An, Q. Li, Z. Luo, L. Che, J. Yang, Z. Chen, W. Zhang, G. Wu, X. Hu, D. Xie, K. Yuan and X. Yang, Electronically Excited OH Super-rotors from Water Photodissociation by Using Vacuum Ultraviolet Free-Electron Laser Pulses, *J. Phys. Chem. Lett.*, 2020, **11**, 7617–7623.

25 L. V. Berkner and L. C. Marshall, Limitation on Oxygen Concentration in a Primitive Planetary Atmosphere, *J. Atmos. Sci.*, 1966, **23**, 133–143.

26 C. E. Harman, E. W. Schwieterman, J. C. Schottelkotte and J. F. Kasting, Abiotic O$_2$ levels on planets around F, G, K, and M stars: Possible false positives for life?, *Astrophys. J.*, 2015, **812**, 137.

27 S. Seager and W. Bains, The search for signs of life on exoplanets at the interface of chemistry and planetary science, *Sci. Adv.*, 2015, **1**, e1500047.

28 R. Hu, S. Seager and W. Bains, Photochemistry in terrestrial exoplanet atmospheres. I. Photochemistry model and benchmark cases, *Astrophys. J.*, 2012, **761**, 166.

29 T. N. Woods, Validation of the UARS solar ultraviolet irradiances: Comparison with the ATLAS 1 and 2 measurements, *J. Geophys. Res.: Atmos.*, 1996, **101**, 9541–9569.

30 A. Bieler, K. Altwegg, H. Balsiger, A. Bar-Nun, J. J. Berthelier, P. Bochsler, C. Briois, U. Calmonte, M. Combi, J. De Keyser, E. F. Van Dishoeck, B. Fiethe, S. A. Fuselier, S. Gasc, T. I. Gombosi, K. C. Hansen, M. Hässig, A. Jäckel, E. Kopp, A. Korth, L. Le Roy, U. Mall, R. Maggiolo, B. Marty, O. Mousis, T. Owen, H. Rème, M. Rubin, T. Sémon, C. Y. Tzou, J. H. Waite, C. Walsh and P. Wurz, Abundant molecular oxygen in the coma of comet 67P/Churyumov-Gerasimenko, *Nature*, 2015, **526**, 678–681.

31 J. Crovisier, The photodissociation of water in cometary atmospheres, *Astron. Astrophys.*, 1989, **213**, 459–464.

32 M. C. Festou, H. Rickman and R. M. West, Comets - II. Models, evolution, origin and outlook, *Astron. Astrophys. Rev.*, 1993, **5**, 37–163.

33 D. G. Goodwin, R. L. Speth, H. K. Moffat and B. W. Weber, *Cantera: An Object-oriented Software Toolkit for Chemical Kinetics, Thermodynamics, and Transport Processes*, 2009.

34 T. I. Hasegawa, E. Herbst and C. M. Leukng, Models of gas-grain chemistry in dense interstellar clouds with complex organic molecules, *Astrophys. J., Suppl. Ser.*, 1992, **82**, 167.

This journal is © the Owner Societies 2021

Phys. Chem. Chem. Phys., 2021, **23**, 9235–9248 | 9247

35 S. Ranjan, E. W. Schwieterman, C. Harman, A. Fateev, C. Sousa-Silva, S. Seager and R. Hu, Photochemistry of Anoxic Abiotic Habitable Planet Atmospheres: Impact of New H$_2$O Cross Sections, *Astrophys. J.*, 2020, **896**, 148.

36 M. W. Claire, J. Sheets, M. Cohen, I. Ribas, V. S. Meadows and D. C. Catling, The evolution of solar flux from 0.1 nm to 160 μm: Quantitative estimates for planetary studies, *Astrophys. J.*, 2012, **757**, 95.

37 T. Turányi, Sensitivity analysis in chemical kinetics, *Int. J. Chem. Kinet.*, 2008, **40**, 685–686.

38 A. Saltelli, K. Chan and E. Scott, *Sensitivity Analysis*, John Wiley, Chichester, NY, 2000.

39 D. D. Y. Zhou, M. J. Davis and R. T. Skodje, Multitarget global sensitivity analysis of n-butanol combustion, *J. Phys. Chem. A*, 2013, **117**, 3569–3584.

40 Y. Chang, Y. Yu, F. An, Z. J. Luo, D. H. Quan, X. Zhang, X. X. Hu, Q. M. Li, J. Y. Yang, Z. C. Chen, L. Che, W. Q. Zhang, G. R. Wu, D. Q. Xie, M. N. R. Ashfold, K. J. Yuan and X. M. Yang, *Nat. Commun.*, 2021, DOI: 10.1038/s41467-021-22824-7.

9248 | *Phys. Chem. Chem. Phys.*, 2021, **23**, 9235–9248

This journal is © the Owner Societies 2021